Center-of-Gravity Placement Effects on a Bio-Inspired Flapping-Wing MAV: An Empirical Characterization for Sensor Payload Integration

I. Guerra Bello[1], A. Lopez[2]*, and M. Gallo[1]
[1]Inholland University of Applied Sciences, Delft, the Netherlands
[2]TU Delft, MAVLab, Delft, the Netherlands

http://www.imavs.org/

Abstract

Autonomous aerial inspection of commercial greenhouses requires a micro air vehicle (MAV) capable of flying close to the canopy while carrying a sensing payload for pest detection. The Flapper Nimble+, a bio-inspired flapping-wing MAV, is well suited to this role, but integrating sensors onto the platform is non-trivial: every control moment is generated through the wings, so even a small shift in the centre of gravity (CG) changes the trim the controller must hold and the way the airframe oscillates. Without quantitative guidance on where payload mass may be placed, integration is reduced to trial and error. We report a systematic two-axis CG-placement campaign on the Nimble+ in which mass was swept along the fore–aft and vertical body axes across 23 configurations and 64 hovering flights, logged simultaneously from onboard flight-controller (FC) telemetry and an external motion-capture system. Two robust empirical relations emerge: steady-state pitch trim varies near-linearly with fore–aft CG offset at -0.97 deg/mm, and body-pitch oscillation amplitude rises near-linearly with the magnitude of vertical CG offset at $+0.60$ deg/mm. These relations give designers a placement rule: keep the payload CG close to the bare-platform CG fore–aft to minimise trim demand, and with minimal vertical offset from it to minimise oscillation. An integrated sensing build assembled for greenhouse inspection confirms the fore–aft relation: its measured pitch-trim shift matches the prediction to within the bare-platform flight-to-flight spread. The vertical relation is corroborated in direction but, owing to the larger variability of the oscillation amplitude, is less precisely predictive. A mount-position imaging experiment shows that placing the camera close to the CG improves detection rate by a factor of 1.78.

*Email: a.p.lopez@tudelft.nl

1 Introduction

Commercial greenhouse crops must be inspected for pests at the founding-colony stage, before an infestation spreads – yet this early detection is hard to achieve with current methods. Pest infestations in high-density plantings of tomato, cucumber and sweet bell pepper are most effectively controlled by biological agents deployed before a colony reaches damaging density, yet the dominant monitoring methods – periodic manual scouting and passive sticky traps – are too infrequent and too coarse to catch a founding colony reliably [1]. Ground robots have been developed for greenhouse tasks but are constrained to row-level access and cannot inspect elevated canopy zones or leaf undersides where many pests establish [2]. An aerial platform that can fly close to the canopy, cover a full corridor pass, and carry a camera capable of resolving pest clusters would close this gap.

The Flapper Nimble+, a bio-inspired flapping-wing MAV, is well suited to this role: its flapping produces lower downwash and a lower acoustic profile than rotary-wing alternatives, reducing disturbance to foliage during close-range operation; its light wings pose little risk of damaging crops or greenhouse structure on incidental contact. It has been demonstrated in a greenhouse environment carrying a camera for pest detection, though that work concluded that a lighter, better-integrated payload was needed [3]. Integrating sensors onto the platform is, however, non-trivial [4]. The Nimble+ generates every control moment through its wings alone [5], so the CG position appears as a parameter in every rotational equation of motion. Adding a sensor payload simultaneously increases total mass and shifts the CG, and the shift is the subtler effect: a few millimetres changes the trim the controller must hold and the amplitude at which the airframe oscillates [6, 7], directly affecting both flight endurance and the quality of images the payload can capture. While the control physics of the platform is established [5], no quantitative guidance exists for how much a given CG shift costs in trim or oscillation on the Nimble+, leaving sensor integration as trial and error.

This paper provides that guidance. We report a systematic two-axis CG-placement campaign and derive two empirical relations that form a bounded predictive model for any payload configuration within the tested envelope. We validate the

http://www.imavs.org/

model against a fully integrated sensing build for greenhouse inspection – quantitatively for the fore–aft trim relation and directionally for the vertical oscillation relation – and show, through a mount-position imaging experiment, that the same CG placement that minimises trim cost also maximises in-flight camera detection rate.

2 PLATFORM AND MOMENT GENERATION

The Flapper Nimble+ is a bio-inspired flapping-wing MAV with a published payload capacity of 25 g above an all-up mass of roughly 102 g,a hover wing-beat frequency of approximately 14-17 Hz, a 5 V / 400 mA payload rail, and an onboard Crazyflie Bolt 1.1 flight controller running a PID stabilisation loop [8]. The platform descends from the DelFly lineage [9] and carries no tail surface: all three-axis control torque is produced through differential wing kinematics via four inputs [5]: left- and right-wing flapping frequencies f_L and f_R, symmetric dihedral angle Γ, and yaw wing-root deflection δ_ψ. The body axis convention is shown in Figure 1: Y along the wing leading edge (LE), Z along the spine, X out of the wing plane.

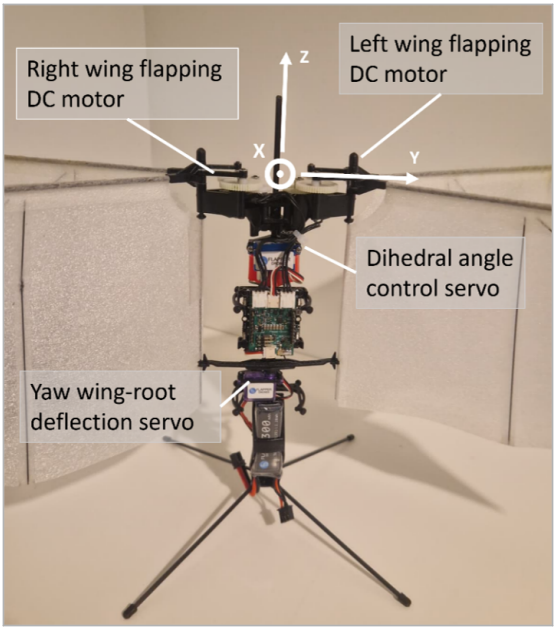

Figure 1: Body axis convention and control actuators of the Flapper Nimble+.

Because the platform is tailless, every control moment equals an aerodynamic force times its arm to the CG [5]. For pitch, the dihedral servo tilts the flapping plane about a hinge ahead of the CG, displacing the thrust vector by $r_x \sin\Gamma$, giving

$$\tau_\Gamma = T\, r_x \sin\Gamma, \tag{1}$$

where T is hover thrust and r_x the fore–aft arm from CG to hinge. A forward CG shift reduces r_x, weakening pitch authority and requiring a larger Γ to hold trim [10] — the physical origin of the sensitivity characterised in Section 4. Roll uses the lateral wing offsets; yaw uses asymmetric wing-root twist. In every case the control moment depends on the CG-to-force arm, so any payload shift changes that arm and propagates into trim, oscillation, and ultimately the quality of the captured imagery.

3 CG SWEEP METHODOLOGY

3.1 Test environment and flight protocol

All flights were conducted in the CyberZoo, a $10\times10\times7$ m enclosed flight volume at TU Delft equipped with an OptiTrack motion-capture (MoCap) system at up to 180 Hz. Every flight was logged by two independent streams: the MoCap returning aircraft position and attitude from infrared markers, and the onboard FC telemetry logging attitude estimates, gyro rates, motor commands and battery state at 50 Hz.

The FC runs a PID stabilisation loop using a downward time-of-flight (ToF) sensor for altitude hold and the onboard IMU for attitude. Pitch and yaw received no pilot input throughout the campaign, so both channels reflect the controller's unforced response to each CG condition. A free-hover protocol was used: the aircraft was launched from one corner and allowed to drift forward under its natural pitching bias, with the pilot giving only occasional lateral corrections to stay within the volume.

Each configuration was flown three times on a single fully charged battery, holding state-of-charge effects constant within a configuration. The campaign spanned several days; on each day the unmodified bare-platform (BASE) configuration was re-flown first and used as that session's reference, ensuring all comparisons are within-session.

3.2 CG mounts and tested configurations

CG offsets were imposed using 3D-printed mass-mount brackets (Figure 2). Front and aft brackets bolted to the FC imposed fore–aft (X) offsets; a top disc and a bottom washer stack imposed vertical (Z) offsets. Each configuration's CG was computed analytically from bench-weighed masses and CAD-extracted mount centroids. Pure single-axis displacement is geometrically impossible, so each configuration carries a small residual in the orthogonal axis; these are used explicitly in the cross-axis checks of Section 4.

The X-sweep covered 14 configurations spanning $\Delta X_{CG} \in [-1.75, +2.86]$ mm (0–11.8 g added mass). The Z-sweep covered 9 configurations spanning $\Delta Z_{CG} \in [-17.55, +10.87]$ mm (0–19.8 g); the vertical range is intentionally exaggerated to map the limits of the relation. Both sweeps are summarised in Table 1.

3.3 Per-flight metrics

The two data streams originate from independent clocks and are processed separately. For each flight a hover window is extracted by isolating the in-flight segment and trim-

http://www.imavs.org/

Figure 2: Mass-mount brackets: fore–aft sweep (front (right) and aft (left) brackets) and vertical sweep (top disc and bottom washer stack).

ming take-off and landing transients; flights with fewer than 15 s of retained data are excluded. From the FC telemetry three metrics are derived. The mean pitch trim $\overline{\theta}_p$ is the time-averaged body pitch, capturing the steady-state attitude the controller settles on. The pitch servo is driven by a pulse-width-modulation (PWM) command m_1. The pitch-servo total variation

$$\mathrm{TV}_{m1} = \frac{1}{T_{\mathrm{hov}}} \sum_{i=1}^{N-1} \left| m_1[i{+}1] - m_1[i] \right| \ [\mathrm{PWM\,s^{-1}}] \qquad (2)$$

Sweep	Configs	Δ_{CG} range (mm)	Mass (g)
X (fore–aft)	14	-1.75 to $+2.86$	0–11.8
Z (vertical)	9	-17.55 to $+10.87$	0–19.8

Table 1: CG-sweep ranges; each configuration flown three times.

measures cumulative pitch-servo effort per second. The servo reversal rate

$$\nu_{\mathrm{cross}} = \frac{1}{T_{\mathrm{hov}}} \sum_{i=1}^{N-1} \mathbf{1}\left[(m_1[i]{-}m_1^*)(m_1[i{+}1]{-}m_1^*) < 0 \right] \ [\mathrm{s^{-1}}] \qquad (3)$$

counts zero-crossings of the servo-neutral reference m_1^* per second and is sensitive to the direction of any trim bias. From the MoCap quaternion, body pitch is derived and the oscillation amplitude σ_{θ_p} is computed as the standard deviation of the mean-removed pitch signal. The extended-Kalman-filter (EKF) smoothed FC signal is used for $\overline{\theta}_p$ and servo metrics; the unfiltered MoCap signal is used for σ_{θ_p}.

4 Results

4.1 *Fore–aft axis: pitch-trim demand*

Of the X-sweep configurations, 38 valid FC flights and 40 valid MoCap flights passed the hover-window filters. The primary finding is a near-linear relationship between per-flight mean body pitch and ΔX_{CG} (Figure 3). An ordinary least-squares (OLS) fit to the per-configuration means gives

$$\overline{\theta}_p(\Delta X_{CG}) = -1.86 - 0.97\,\Delta X_{CG} \quad [\mathrm{deg}], \qquad (4)$$

with Pearson correlation coefficient $r = -0.97$: approximately one degree of nose-up trim per millimetre of forward CG shift. The -1.86 deg intercept is the residual trim of this build at $\Delta X_{CG} = 0$.

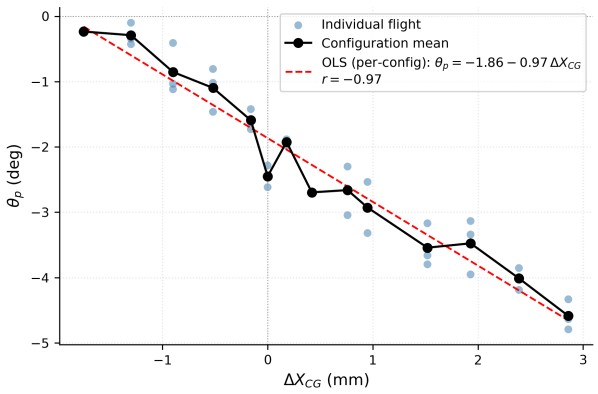

Figure 3: Per-flight mean body pitch vs. ΔX_{CG}. Dots are individual flights; connected points are per-configuration means; dashed line is the OLS fit of Equation 4.

The pitch-axis control activity provides independent corroboration (Figure 4). TV_{m1} rises away from $\Delta X_{CG} = 0$ in both directions, the expected signature of the servo doing more total work as $|\Delta X_{CG}|$ grows. ν_{cross} behaves asymmetrically: forward CG biases m_1 above neutral so zero-crossings become rare even as TV_{m1} peaks; at the aft extreme the trim approaches neutral and reversals are highest. This asymmetry is the control-side fingerprint of Equation 4,

read from the raw PWM stream without passing through the state estimator.

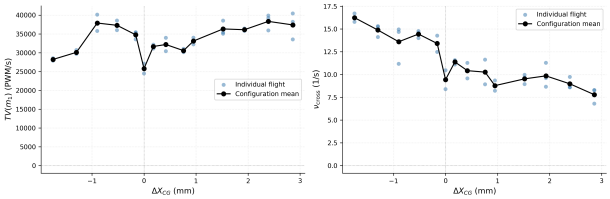

Figure 4: Pitch-servo total variation (left) and reversal rate (right) vs. ΔX_{CG}. Both independently corroborate the trim relation.

A cross-axis check confirms the relation is fore–aft specific. Mean pitch from the Z-sweep varies by only $\sim$1.4 deg across the full $\pm$17 mm vertical range, consistent with the small residual ΔX_{CG} carried by the Z mounts propagated through Equation 4. Vertical CG placement does not drive steady-state pitch trim.

4.2 *Vertical axis: pitch-oscillation amplitude*

Of the Z-sweep configurations, 26 valid FC flights and 21 valid MoCap flights passed the filters.

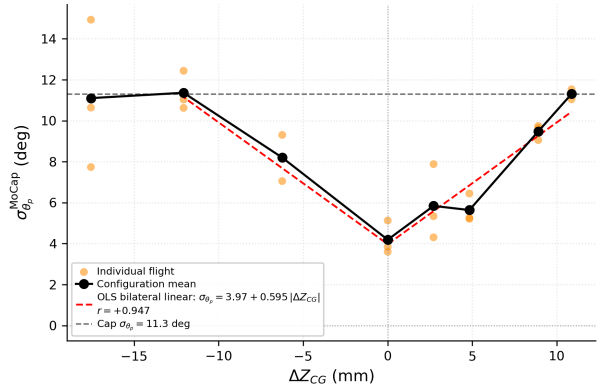

Figure 5: Pitch-oscillation amplitude vs. ΔZ_{CG}. Dashed line: bilateral OLS fit; horizontal dashed line: saturation cap.

Figure 5 shows a bilateral, near-monotonic rise in σ_{θ_p} with $|\Delta Z_{CG}|$. The per-configuration means rise from $\sigma_{\theta_p} \approx 4.2$ deg at $\Delta Z_{CG} = 0$ to about 11.3 deg at both vertical extremes, a near-threefold increase on both sides. The rise is bilateral: vertical offsets above and below the bare-platform CG both amplify the oscillation.

Because the platform is flown closed-loop, what is measured is the combined response of the airframe and its PID stabilisation loop rather than the airframe alone, and two effects plausibly contribute. The vertical offset alters the arms and inertia through which the wings generate the pitch moment, and the PID, tuned to the bare-platform response, applies the same commands to an airframe that now reacts differently and so operates away from its tuning point. Separating the two would require closed-loop system identification, which was outside this campaign. What the data shows unambiguously is that vertical CG displacement in either direction amplifies pitch oscillation. An OLS fit gives

$$\sigma_{\theta_p}^{\text{pred}}(\Delta Z_{CG}) = \min\big(3.97 + 0.595|\Delta Z_{CG}|,\ 11.3\big)\ [\text{deg}], \tag{5}$$

with $r = +0.95$ and a saturation cap at 11.3 deg. The single slope on $|\Delta Z_{CG}|$ is treated as an empirical engineering fit, justified by the symmetric, bilateral response noted above rather than by a single physical mechanism. The vertical brackets also add mass with $|\Delta Z_{CG}|$ (up to $\sim$19% of body mass), and the resulting parallel-axis inertia increase is small by comparison ($\sim$0.6–1.8% of $I_{yy,0} = 3.35 \times 10^{-4}$ kg m^2 [8] at the sweep extremes), so Equation 5 is best read as a fit to mass-and-offset-coupled configurations rather than a pure CG-height effect, which is a further reason the vertical relation is confirmed in direction but not tightly in magnitude.

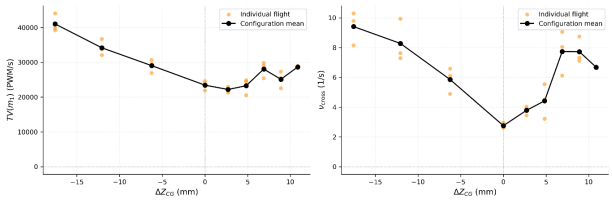

Figure 6: Pitch-servo total variation (left) and reversal rate (right) vs. ΔZ_{CG}.

Servo activity corroborates this: both TV_{m1} and ν_{cross} rise away from $\Delta Z_{CG} = 0$, steeper on the lower side. A cross-axis check shows σ_{θ_p} varying by only $\sim$3 deg across the fore–aft range, confirming that pitch-oscillation amplitude is vertically driven and fore–aft independent.

5 Trim Model

Equations 4 and 5 are packaged into a simple payload-placement model. The system CG is computed by mass-weighted combination of the bare-platform CG with the payload-component centroids; each component is treated as a point mass (its own area moment is one to two orders of magnitude below the parallel-axis contribution [5]), and the inertia tensor is updated about the new CG. The model returns predicted pitch trim and oscillation amplitude, valid within the tested envelope:

$$\begin{aligned} -1.75 \le \Delta X_{CG} \le +2.86\ \text{mm}, \\ -17.55 \le \Delta Z_{CG} \le +10.87\ \text{mm}. \end{aligned} \tag{6}$$

Configurations outside this envelope are flagged as unsupported extrapolations. A compact inspection payload sits well inside both bounds. Of the two outputs, the pitch-trim prediction is the quantitatively reliable one; the oscillation ampli-

http://www.imavs.org/

http://www.imavs.org/

tude should be read as an indicative magnitude and a dependable indicator of trend rather than a tight point prediction.

6 Integrated-Payload Comparison

To test the model against a real build, a sensing configuration was assembled: an OpenMV AE3 global-shutter camera (1 MP, 120 fps, 5 g, integrated 8×8 ToF sensor & IMU), a downward optical-flow/ToF sensor, and a ultra-wideband (UWB) positioning deck + ToF sensor pack, totalling 15.1 g. The build shifts the system CG by $\Delta X_{CG} = -1.32$ mm and $\Delta Z_{CG} = -0.69$ mm (1.50 mm total), which sits inside the envelope of Equation 6.

The integrated build and the bare platform were each flown six times under the same free-hover protocol. Table 2 compares the model-predicted change (integrated minus bare) against the measured within-session change. Because the bare-platform trim baseline drifts between sessions, only within-session deltas are compared; the relation is predictive on the deltas despite this baseline drift.

Quantity	Predicted Δ	Measured Δ	Residual
Pitch trim (deg)	+1.29	+1.11	−0.18
Pitch oscillation (deg)	+0.41	+0.83	+0.42

Table 2: Model-predicted versus measured within-session change (integrated minus bare platform), second test session, $n = 6$ bare and $n = 6$ integrated flights (oscillation row: $n = 5$ bare, one flight excluded for a motion-capture tracking fault).

Predicted and measured pitch trim agree in sign and magnitude: the model predicts a +1.29 deg nose-up shift for the −1.32 mm aft CG offset, against a measured +1.11 deg, a residual (−0.18 deg) within the bare-platform flight-to-flight spread ($\sigma = 0.19$ deg). The integrated build therefore does not measurably degrade static stability, and the trim relation of Equation 4 carries over from the controlled sweep to a real build.

The oscillation row of Table 2 is reported for completeness but is a weak test of Equation 5: the build's vertical CG shift is small ($\Delta Z_{CG} = -0.69$ mm), so the predicted change (+0.41 deg) is itself comparable to the flight-to-flight scatter. The measured amplitude rose by +0.83 deg, in the predicted direction but overshooting the prediction, which is consistent with the oscillation relation being established by the full ±17 mm sweep of Section 4 rather than by this near-centred build. This is the expected asymmetry between the two relations: fore–aft trim is predicted to within its flight-to-flight spread, whereas vertical oscillation amplitude is confirmed in direction but not closely in magnitude.

6.1 Camera mount position and detection rate

So far CG placement has been treated as a flight-performance question. It is also a sensor-performance question: where the camera sits relative to the CG sets how much of the airframe's pitch motion affects image acquisition via motion blur.

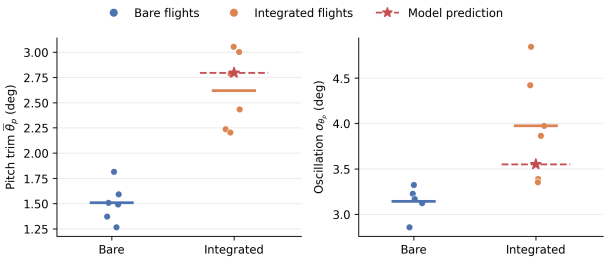

Figure 7: Integrated-build validation. For each quantity, bare-platform (blue) and integrated-build (orange) per-flight values are shown with their means (horizontal bars); the red star marks the model-predicted integrated value (bare mean plus predicted change). Trim matches the prediction within scatter; oscillation rises as predicted in direction but overshoots in magnitude.

To show this, the AE3 camera was flown over a fixed AprilTag target during hover in two mounting positions (Figure 8). In the first the camera sits close to the system CG; in the second it is mounted about 20 mm lower, at a longer arm from the CG.

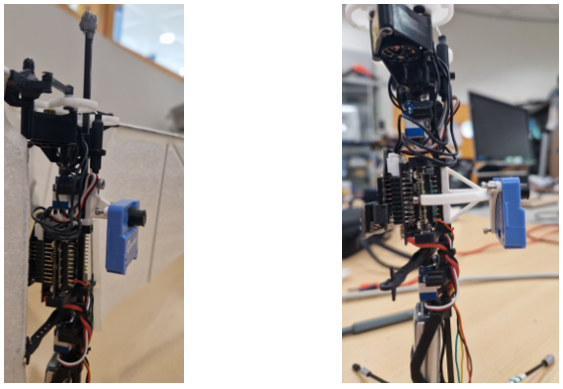

Near-CG mount Below-CG mount

Figure 8: Side views of the two camera mounting positions tested. The near-CG mount (left) places the camera close to the system CG; the below-CG mount (right) places it about 20 mm lower.

What sets the two mounts apart is the magnitude of the total CG shift from the bare-platform reference: 1.16 mm for the near-CG mount and 2.70 mm for the below-CG mount, about 2.3× larger. Tag detections were extracted offline over the in-window hover frames. The near-CG mount detected the tag in 24.3% of frames against 13.6% for the below-CG mount, a factor of 1.78.

At a larger arm l from the CG, a given body angular rate ω produces a proportionally larger linear velocity at the im-

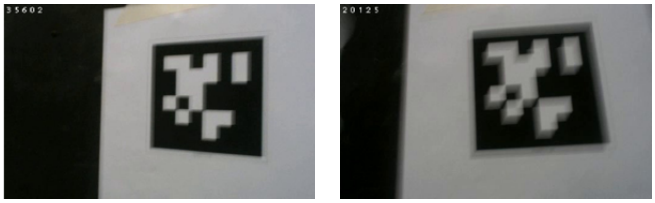

Near-CG mount Below-CG mount

Figure 9: Flying image results from the two mounts. Near the CG (left), below the CG (right)

age plane ($v \approx \omega l$), so the below-CG camera sweeps more image motion into each frame and blurs a larger fraction of them. In short, the larger the body angular rate the camera experiences, the more it degrades the captured image; mounting the camera close to the CG therefore minimises this image-plane motion and maximises detection rate, the same placement that minimises trim demand. Figure 9 shows this directly – the same tag imaged sharply from the near-CG mount and smeared from the below-CG mount.

7 CONCLUSION

We characterised how centre-of-gravity placement affects flight on a bio-inspired flapping-wing MAV through a controlled two-axis mass-placement sweep on the Flapper Nimble+. Fore–aft CG offset drives steady-state pitch trim near-linearly at -0.97 deg/mm ($r = -0.97$), and vertical CG offset drives pitch-oscillation amplitude at $+0.60$ deg/mm ($r = +0.95$); each relation is corroborated by independent servo-activity metrics and confirmed axis-specific by cross-axis checks. The reported slopes and intercept are calibration constants of this specific airframe and should not be transferred numerically to other platforms; what is expected to generalise is the underlying mechanism – CG-referenced pitch trim scaling and vertical-offset-driven oscillation (Equation 1) – rather than its magnitude, consistent with qualitatively similar CG sensitivities reported for other tailless FW-MAVs [6, 7]. Packaged as a bounded linear model, the fore–aft relation predicts the pitch trim of an integrated greenhouse-inspection build to within the bare-platform flight-to-flight spread, validating it as a quantitative placement tool. The vertical relation is confirmed in direction–oscillation amplitude rises with vertical CG offset in both the sweep and the integrated build–but its larger flight-to-flight variability makes the precise amplitude harder to predict, so it is best used as a bounded trend. The practical rule is direct: place payload mass close to the bare-platform CG fore–aft to minimise trim demand, and with minimal vertical offset from it to minimise oscillation. Future work centres on tightening the oscillation prediction through an expanded integrated-build campaign under a stabilised position hold and closed-loop system identification, alongside a payload-aware feedforward trim schedule and autonomous corridor flight with the integrated build inside a commercial greenhouse.

ACKNOWLEDGEMENTS

This publication is part of the project 'Bio-inspired Micro Aerial Vehicle for sustainable pest control in horticulture – Flappy', with file number RAAK.PRO04.081, of the research program RAAK-PRO, which is financed by Regieorgaan SIA, part of the Netherlands Organisation for Scientific Research (NWO).

REFERENCES

[1] J.C. van Lenteren. The state of commercial augmentative biological control: plenty of natural enemies, but a frustrating lack of uptake. *BioControl*, 57(1):1–20, 2012.

[2] C.W. Bac, E.J. van Henten, J. Hemming, and Y. Edan. Harvesting robots for high-value crops: state-of-the-art review and challenges ahead. *Journal of Field Robotics*, 31(6):888–911, 2014.

[3] O. Awesta, V. Hollink, and M. Gallo. Flapping-wing drones for pests and diseases detection in horticulture. *IEEE Transactions on AgriFood Electronics*, pages 1–10, 2025.

[4] M.L. Afakh, A.A. Saputra, H. Sato, K. Wada, and N. Takesue. Servo-driven flapping-wing aerial vehicle (FWAV): Payload capacity and navigation performance. In *2025 IEEE/SICE International Symposium on System Integration (SII)*, pages 1071–1076, 2025.

[5] M. Karásek, F.T. Muijres, C. De Wagter, B.D.W. Remes, and G.C.H.E. de Croon. A tailless aerial robotic flapper reveals that flies use torque coupling in rapid banked turns. *Science*, 361(6407):1089–1094, 2018.

[6] L.T.K. Au and H.C. Park. Influence of center of gravity location on flight dynamic stability in a hovering tailless FW-MAV: Longitudinal motion. *Journal of Bionic Engineering*, 16(1):130–144, 2019.

[7] L.T.K. Au and H.C. Park. Influence of center of gravity location on flight dynamic stability in a hovering tailless FW-MAV: Lateral motion. *Journal of Bionic Engineering*, 17:148–160, 2020.

[8] Flapper Drones. Nimble+ specifications and documentation, 2026. `https://docs.flapper-drones.eu`.

[9] G.C.H.E. De Croon, M.A. Groen, C. De Wagter, B. Remes, R. Ruijsink, and B.W. Van Oudheusden. Design, aerodynamics and autonomy of the DelFly. *Bioinspiration & Biomimetics*, 7(2):025003, 2012.

[10] E. Sanchez-Laulhe, G.C.H.E. de Croon, and A. Ollero. Equilibrium state for a tailless flapping wing micro air vehicle in forward flight. *IEEE Robotics and Automation Letters*, 11(1):17–24, 2026.

http://www.imavs.org/